J. Mech. Phys. Solids 99 (2017) 357–378

Contents lists available at ScienceDirect

Journal of the Mechanics and Physics of Solids

journal homepage: www.elsevier.com/locate/jmps

Numerical study of adhesion enhancement by composite fibrils with soft tip layers

Ram Gopal Balijepalli[a,b], Sarah C.L. Fischer[a,b], René Hensel[a], Robert M. McMeeking[a,c,d], Eduard Arzt[a,b,*]

[a] INM – Leibniz Institute for New Materials, Campus D2 2, Saarbrücken, Germany
[b] Department of Materials Science and Engineering, Saarland University, Campus D2 2, Saarbrücken, Germany
[c] Materials and Mechanical Engineering Departments, University of California, Santa Barbara, CA 93106, USA
[d] Engineering School, University of Aberdeen, King's College, Aberdeen AB24 3UE, UK

A B S T R A C T

Bio-inspired fibrillar surfaces with reversible adhesion to stiff substrates have been thoroughly investigated over the last decade. In this paper we propose a novel composite fibril consisting of a soft tip layer and stiffer stalk with differently shaped interfaces (flat vs. curved) between them. A tensile stress is applied remotely on the free end of the fibril whose other end adheres to a rigid substrate. The stress distributions and the resulting adhesion of such structures were numerically investigated under plane strain (2*D*) and axisymmetric (3*D*) conditions. The stress intensities were evaluated for different combinations of layer thickness and Young's moduli. The adhesion strength values were found to increase for thinner layers and larger modulus ratio; these trends are also reflected in selected experimental results. The results of this paper provide a new strategy for optimizing adhesion strength of fibrillar surfaces.

1. Introduction

Nature provides many concepts for temporary and reversible adhesion to various substrates, e.g. on plants and animals (Gorb, 2007, 2008). Geckos and insects use hairy structures whose adhesion is due to intermolecular forces (Arzt et al., 2003; Autumn et al., 2000, 2002; Gao et al., 2005; Huber et al., 2005). Transferring nature's solution into artificial structures that may eventually find technological applications is the current objective of research and development efforts (Boesel et al., 2010; Kamperman et al., 2010; Menon et al., 2004; Purtov et al., 2015; Sathya et al., 2013). Many reversible attachment systems (Paretkar et al., 2011) based on micropatterns (del Campo and Arzt, 2011) have been investigated in the literature (Arzt et al., 2002; Barreau et al., 2016; del Campo and Arzt, 2007; Greiner et al., 2009; Mengüç et al., 2012; Spolenak et al., 2005).

Recent modelling studies have pointed to the importance of optimizing the distribution of interfacial stresses in order to realize high adhesion. Following biological examples, fibrils with spatula and mushroom-shaped tips have repeatedly been demonstrated to exhibit superior adhesion performance (del Campo et al., 2007; Gorb et al., 2007; Greiner et al., 2007; Kim and Sitti, 2006). Numerical simulations have suggested that the main reasons for improved adhesion is the reduction of the stress magnitudes associated with the corner singularity, which is likely to act as a crack initiation point in straight homogeneous punch (SHP) fibrils (Khaderi et al., 2015). Spuskanyuk et al. (Spuskanyuk et al., 2008) showed numerically that in mushroom fibrils the edge stresses were significantly reduced when compared to those of SHP and other shapes. Based on earlier work by Akisanya and Fleck (1997)

* Corresponding author at: INM – Leibniz Institute for New Materials, Campus D2 2, Saarbrücken, Germany.
E-mail address: progress@leibniz-inm.de (E. Arzt).

http://dx.doi.org/10.1016/j.jmps.2016.11.017
Received 16 September 2016; Received in revised form 8 November 2016; Accepted 17 November 2016
Available online 01 December 2016

and Khaderi et al. (2015) on the corner stress singularity, we have recently addressed the stress distributions of mushroom fibrils (Balijepalli et al., 2016). In an extensive parametric study, we showed that such structures benignly distribute tractions along the interface and reduce the magnitude of the stresses associated with the singularity at the corner. This is suggested to be the main cause of the higher adhesion of mushroom structures while the onset of detachment is shifted away from the corner to the centre of the interface (Aksak et al., 2014; Balijepalli et al., 2016; Carbone and Pierro, 2012).

Mushroom tips are often manufactured by manual inking of previously made microstructures in a prepolymer and subsequent curing in contact with a smooth counter surface (Fischer et al., 2016; Greiner et al., 2007; Murphy et al., 2009; Varenberg and Gorb, 2007). Tip and stalk material can be identical, but choosing a softer tip layer can further increase adhesion, especially to rough and deformable surfaces such as skin (Bae et al., 2013b; Kroner et al., 2012b; Kwak et al., 2011). In related work, Waters et al. (2009) have studied numerically how a slight waviness in the surface can increase the adhesion strength in the JKR regime. Gao and Yao (2004) have shown theoretically that adhesion can be enhanced by optimizing shape and by reducing size. Depending on the packing density and the amount of prepolymer used for the inking, not only isolated tips can be achieved but also connection among several or all fibrils (Liu et al., 2009; Vajpayee et al., 2009). Despite these benefits, mushroom structures suffer from the drawbacks that their fabrication is complicated, does not always lead to reproducible results and can hardly be scaled up to larger areas.

An alternative way to manipulate the interfacial stresses is to create fibres with gradients in mechanical properties (Bae et al., 2013a; Minsky and Turner, 2015; Scholz et al., 2008; Yao and Gao, 2010; Yoon et al., 2011). The ladybug has recently been shown to exhibit attachment hairs with at least two property levels, i.e. a soft tip layer with a modulus of about 1.2 MPa attached to a stiff stalk with a modulus of about 6.8 GPa (Peisker et al., 2013). According to Gorb and Filippov (Gorb and Filippov, 2014) such structures tend to enhance adhesion properties, especially against substrates with unpredictable roughness.

In this paper, we propose a novel two-material composite fibril with a sharp transition in modulus as an alternative to reduce the singularity at the corner. For modelling the stress singularities, the fibril was assumed to have a straight punch shape, but to consist of a comparatively stiff stalk and a soft layer at its tip. A detailed numerical study is presented of the stress distributions along and near differently shaped interfaces between the two materials, as shown in Fig. 1. The system parameters are the Young's moduli (E_1, E_2) and the thicknesses (L_1, L_2) of, respectively, the stalk and the soft tip layer. For comparison, adhesion experiments to glass were performed with single macroscopic composite fibrils.

2. Numerical and experimental methods

2.1. Numerical simulations

A compliant composite fibril, with diameter D and length L, was assumed to adhere to a rigid substrate with no defects (interfacial cracks) along the interface. The ratio of L to D was 2 in all the simulations and experiments, because of practical limitations in the fabrication procedure. The fibril was considered to be an isotropically elastic and incompressible solid. The boundary condition was assigned to be sticking friction which totally suppressed sliding of the fibril against the substrate. A remote stress $\sigma_A$was applied on the free end of the fibril (Fig. 1), which results in a stress singularity at the fibril-substrate interface (Akisanya and Fleck, 1997). The corner singularity method was adopted from (Akisanya and Fleck (1997) and Khaderi et al. (2015). The treatment follows that of our earlier paper on mushroom-shaped fibrils (Balijepalli et al., 2016). The solution based on the detailed asymptotic corner singularity is explained in Appendix A. As seen in Eq. (A10) (Appendix A), the adhesion strength of the composite fibril S^I can be expressed as follows

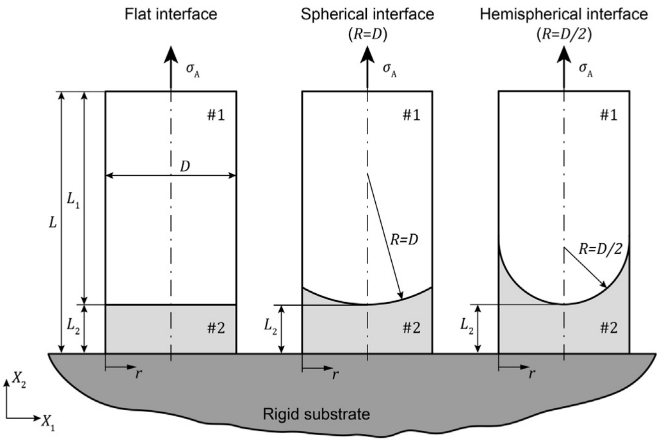

Fig. 1. Schematic of different composite fibril interfaces, namely a flat interface, a spherical ($R = D$), and a hemispherical interfaces ($R = D/2$), considered in the current paper. The parameter R is the radius of curvature of the interface, D is the fibril diameter, L is the total height of the composite fibril,L_1 and L_2 are the thicknesses of the stiff stalk (#1, with modulus E_1) and the soft layer (#2, with modulus E_2) respectively. The composite fibrils adhere to a rigid substrate. For a remote tensile stressσ_A applied on the free end, the normal stress distribution is calculated along the fibril/substrate interface.

$$S^I = \frac{0.6\sqrt{E_2 W}}{D^{0.406} l^{0.094} \tilde{\alpha}}$$

where E_2 is Young's modulus of the soft layer in contact with the rigid substrate, W is the adhesion energy, l is the crack length and $\tilde{\alpha}$ is the calibration coefficient of a composite fibril.

The normalized adhesion strength is defined as (Eq. (A11)): $S^I/S^{punch} = a_1/\tilde{\alpha}$ where S^{punch} is the adhesion strength of the straight homogeneous punch (SHP) and a_1 its calibration coefficient.

Following the expectation that the interfacial stress distribution would be modulated by the geometry of the interface, three different interface shapes were considered, i.e. flat and two spherical interfaces ($R = D$ and $R = D/2$) as shown in Fig. 1. Calculations were performed for plane strain ($2D$) and axisymmetric ($3D$) conditions. Only $3D$ results will be discussed in the main paper while the $2D$ results are presented in Appendix C. For each interface shape, we have examined six different thickness ratios (L_2/L = 0.25, 0.20, 0.15, 0.10, 0.05 and 0.005) and five different Young's modulus ratios (E_1/E_2=2, 10, 10^2, 10^3 *and* 10^6) for all axisymmetric ($3D$) fibrils. For plane strain ($2D$) fibrils only five different thickness ratios (L_2/L = 0.25, 0.20, 0.15, 0.10 and 0.05)and four different Young's modulus ratios (E_1/E_2=2, 10, 10^2 *and* 10^3) were considered. For the simulations, the Poisson's ratio was 0.49999 for all materials in accordance to incompressibility.

A mesh validation study was performed to identify the optimum mesh density and the element size along the interface was chosen such that further mesh refinement did no longer influence the results (within 0.5% in the stress values). We used linear quadrilateral hybrid elements for plane strain (Abaqus terminology element CPE4RH) and axial symmetry (CAX4RH) (Abaqus6.11, 2011). The total number of elements varied accordingly from 100,000 to 600,000 for different investigated geometries. The mesh along the interface was much finer than elsewhere to extract more precise information from this region.

2.2. Fibril fabrication

In addition to the numerical simulation, adhesion was tested in selected experiments on composite fibrils with macroscopic dimensions (diameter 2mm, height ca. 4mm and varying soft layer thickness). The fibrils consisted of a stiff stalk; for this, poly(ethyleneglycol) dimethacrylate (PEGdma, Sigma-Aldrich, St. Louis, MO, USA; E = 350 MPa) or polydimethylsiloxane (PDMS, Sylgard 184, Dow Corning, Midland, MI, USA; E=2 MPa) were used. The softer tip layer consisted of polyurethane Polyguss 74 − 41 (PU, PolyConForm GmbH, Duesseldorf, Germany) with E = 900 kPa. Thus, composites fibril structures with an elastic modulus ratio of stiff to soft of about 350 and 2, and two interface geometries, flat and hemispherical ($R = D/2$), were generated. As control samples, fibrils consisting entirely of PU were manufactured.

The fibrils were fabricated in a two-step moulding process as shown in Fig. 2. In a first step, the stalk of the composite fibril was generated using a custom-made aluminum mould (Fig. 2a). The soft layer was added to the fibril in the second moulding step (Fig. 2b): The second pre-polymer, PU, was applied on top of the fibril and the superfluous polymer was removed. To realize different thicknesses of the soft material, spacers with different thickness were used. Cross-sections of the final fibrils are shown in the optical micrograph in Fig. 2b. A more detailed description of the fabrication will be published elsewhere (Fischer et al., 2016).

2.3. Adhesion experiments

Normal adhesion experiments were performed using a custom-built, slightly modified setup following Kroner et al. (2012a). A nominally flat glass substrate was used as a probe and the specimen was aligned by optical inspection. During the adhesion

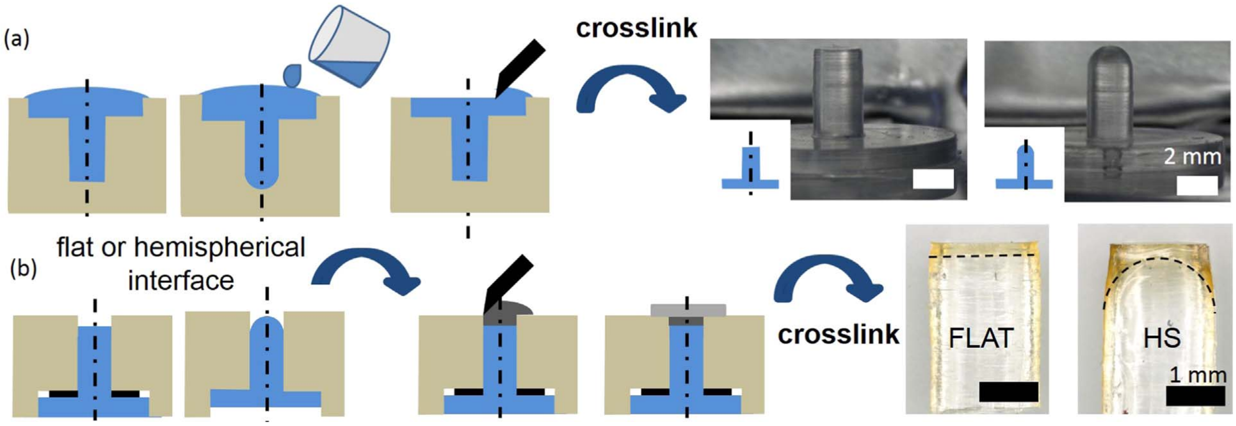

Fig. 2. Two-step manufacturing process of macroscopic composite fibrils. (a) The fibril stalk is manufactured by filling a prepolymer into a mould with a flat or hemispherical (HS) bottom; after the backing layer is flattened using a razor blade, the material is crosslinked. Optical micrographs show exemplary stalk structures. (b) A softer layer is added in a second mould. The layer thickness is determined by spacers (in black). The prepolymer of the soft material is covered with a Teflon coated glass slide (in grey) to obtain a flat surface after crosslinking. Optical micrographs show cross sections of final structures. For a more detailed description see Fischer et al. (2016).

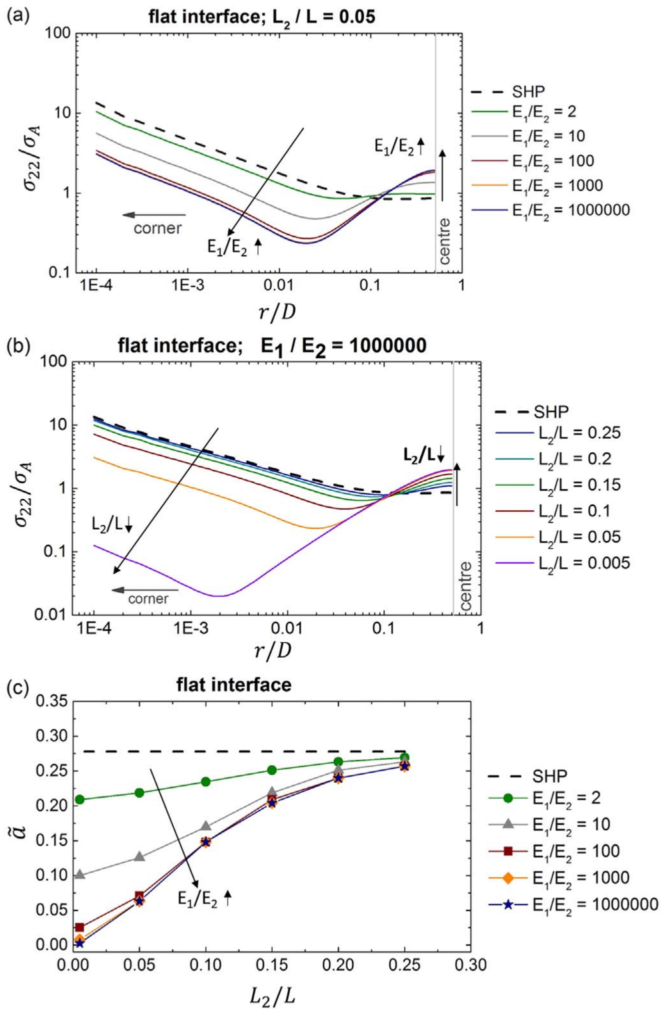

Fig. 3. Analysis of a composite fibril with flat interface (axisymmetric case). (a) Normalized tensile stress σ_{22}/σ_A along the fibril-substrate interface for different Young's modulus ratios E_1/E_2 at constant $L_2/L = 0.05$. (b) Plots for different combinations of L_2/L at constant E_1/E_2=1000000. (c) Calibration coefficient for different combinations of L_2/L and E_1/E_2. The dashed black lines represent the straight homogeneous punch (SHP) results.

measurements, a constant velocity of 5μm/s was maintained. Sample and substrate were brought towards each other until a maximum force, i.e. the preload force, was reached and then moved apart until the sample detached from the substrate. Two different characteristic forces were determined: The pull-off force indicates the maximal force that has to be applied to cause full detachment. However, a crack can propagate in a stable manner along the interface or further cracks can be initiated before delamination takes place. Therefore, the force necessary to initiate the first crack was also determined.

For each sample, five different preloads between 40 to 150 mN were applied and all pull-off forces obtained were averaged. The adhesion measurements were repeated at two different positions on the substrate.

3. Results

3.1. Numerical results

3.1.1. Flat interface

The results for axisymmetric (3*D*) composite fibrils with a flat interface, where the total height of the fibril is twice the diameter (L/D=2), will be presented in this section. The effects of variations in Young's modulus at constant soft layer thickness ($L_2/L = 0.05$) are reported in Fig. 3a. The normal stress along the fibril-substrate interface, normalized by the remote stress, is plotted against the normalized distance from the corner, r/D. It is seen that an increase in E_1/E_2 from 1 to 10^6 leads to a progressive decrease in the magnitude of the corner singularity; at the same time, the stress values at the centre of the fibril increase and reach a maximum value of about 0.3. Further increase beyond the ratio of 1000 no longer affects the stress behaviour significantly, at least for fibrils with $L_2/L = 0.25$ to 0.05. By comparison with the solution for the straight homogeneous punch fibril (shown as a dashed line), all

Table 1
Calibration coefficients $\tilde{a}$ for flat interface for the axisymmetric case.

L_2/L	$\tilde{a}$				
	$E_1/E_2 = 2$	$E_1/E_2 = 10$	$E_1/E_2 = 100$	$E_1/E_2 = 1000$	$E_1/E_2 = 1000000$
0.25	0.2692	0.2630	0.2570	0.2570	0.2570
0.2	0.2630	0.2512	0.2399	0.2399	0.2399
0.15	0.2512	0.2188	0.2089	0.2042	0.2042
0.1	0.2344	0.1698	0.1479	0.1479	0.1479
0.05	0.2188	0.1259	0.0708	0.0631	0.0631
0.005	0.2089	0.1000	0.0251	0.0063	0.0063

composite fibrils exhibit lower corner stresses, at the expense of higher centre stresses. The results for plane strain fibrils are reported in Fig. C3 in Appendix C.

Fig. 3b depicts the influence of the thickness L_2 of the softer material at a constant Young's modulus ratio $E_1/E_2 = 10^6$. It can be seen that L_2 exerts a strong influence on the calculated stress distribution: smaller thicknesses reduce the corner stress more significantly and, again, the centre stresses increase until a maximum value of about 0.3 is reached. The plane strain case is again reported in Fig. C4 in Appendix C. In order to explain the increase of the centre stress, an asymptotic stress analysis was performed (Appendix B). We consider an axisymmetric cylindrical fibril of diameter D adhering to a rigid flat substrate. The fibril is also rigid other than an infinitesimally thin layer of compliant material at the tip where the fibril adheres to the substrate (i.e., $E_1/E_2 \to \infty$ and $L_2/L \to 0$). The solution shows that the tensile stress along the fibril-substrate interface varies with r^2 (Eq. (B31) in Appendix B) and is therefore greatest at the centre of the fibril. Furthermore, the analysis predicts that the tensile stress at the centre is twice as high as the applied stress (Eq. (B34) in Appendix B), which is in good agreement with the numerical solution ($\log \sigma_{22}/\sigma_A \approx 0.3$) obtained for high Young's modulus ratios and very thin soft layers.

The results shown in Fig. 3a and b were fitted with the asymptotic stress solution from Eq. (A3) to find the calibration coefficients $\tilde{a}$ for different combinations of E_1/E_2 and L_2/L (Fig. 3c and Table 1). Plane strain results are reported in Fig. C3 and Table C1 in Appendix C.

3.1.2. Curved interfaces

The normal stress distributions and the calibration coefficients for the two curved interfaces with spherical interface (SI, $R = D$) and hemispherical interface (HSI, $R = D/2$) can be seen in Figs. C4–C7 in Appendix C, respectively, for plane strain and axisymmetric cases. The calibration coefficients are provided in Table C2 in Appendix C for the plane strain (Table C2(a)) and axisymmetric case (Table C2(b)). A comparison for the different interface shapes (FI, SI and HSI) for constant E_1/E_2 ratio of 1000, but two different L_2/L ratios of 0.25 and 0.05, is given in Fig. 4 and the corresponding plane strain comparison can be seen in Fig. C8 in Appendix C. It can be observed that for $L_2/L = 0.25$ the influence of interface shape is insignificant as all curves collapse and approach the SHP case. For thinner soft layers (e.g., $L_2/L = 0.05$), interface shape strongly influences the distribution of stress along the interface: In the case of $R = D$ and $L_2/L = 0.05$, the centre stress is 2.9 times the applied stress (Fig. 4), which is similar to the value of 3.3 calculated analytically (Eq. (B37) in Appendix B). For even thinner soft layers ($L_2/L = 0.005$), the centre stress rises up to 14.1 and 15.2 times the applied stress in the numerical (Fig. C5 in Appendix C) and the analytical solution (Eq. (B37) in Appendix B). Hence, thinner soft layers always lead to higher centre stresses. By increasing the radius of the interface curvature, the corner and the centre stress are slightly reduced. The flat interface is most efficient in reducing both the corner stress and the centre stress.

3.1.3. Adhesion strength

The normalized adhesion strength $S^I/S^{punch}$was calculated by using Eqs. (A10) and (A11) in Appendix A. The result for flat, spherical and hemispherical interfaces and various $L_2/L$and E_1/E_2 ratios are shown in Fig. 5 and Table 2. The corresponding plane strain results for circular interfaces are given in Fig. C9 and Table C3. It is seen that both parameters, which are design parameters for composite fibrils, affect adhesion: smaller layer thicknesses and higher Young's modulus ratios result in higher adhesion strength. Close inspection shows that the interface curvature becomes important only for very thin soft layers ($L_2/L < 0.05$), where the flat interface showed highest adhesion.

3.2. Experimental results

While the stress distribution along the substrate-fibril interface is not directly accessible in experiments, the adhesion strength was defined as the normal pull-off force divided by the total apparent contact area of $A = 3.14\text{mm}^2$. The adhesion performance of a SHP fibril and one with a flat interface and a hemispherical interface ($R = D/2$) for two elastic modulus ratios E_1/E_2=2 and 350 were studied. By dividing the adhesion strengths of the composites by those of the SHP fibril, a normalization was achieved for direct comparison with the numerical results.

The normalized adhesion strengths for flat and hemispherical interface structures are shown in Fig. 6 along with the predictions from the numerical simulations for very similar Young's modulus ratios. Each point in the graph represents the average value of all measurements performed with one sample, the errors being smaller than the symbol size. The absolute pull-off forces measured for

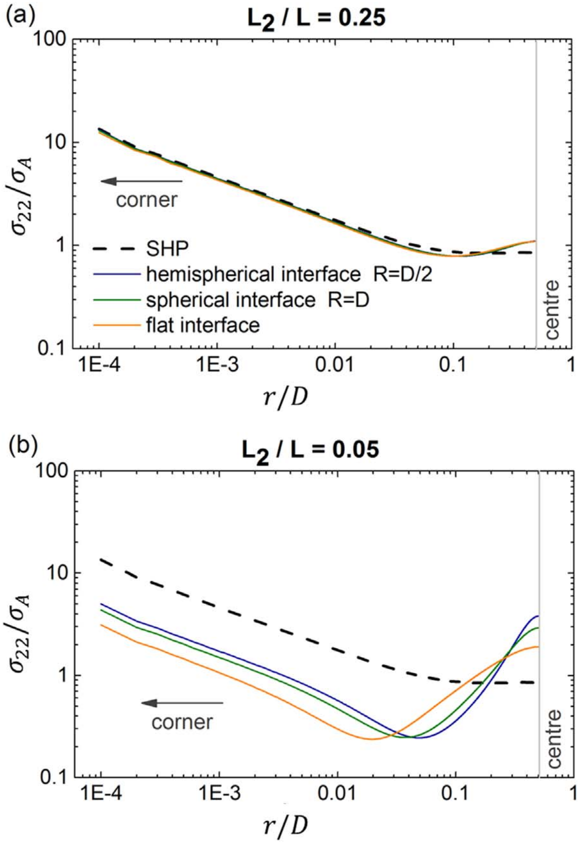

Fig. 4. Normalized stress σ_{22}/σ_A along the fibril-substrate interface for fibrils with different interface curvatures, E_1/E_2=1000 and (a) L_2/L= 0. 25 and (b) L_2/L = 0.05. The dashed black lines represent the straight homogeneous punch (SHP) results.

the composite fibrils were always higher than for the reference fibril made entirely from the soft material (i.e., the SHP case). Two regimes of the experimental data can be distinguished:

3.2.1. *Regime of large soft layer thickness*

Provided $L_2/L > 0.06$ for E_1/E_2=350 and $L_2/L > 0.03$ for E_1/E_2=2, the measured adhesion strength increased with decreasing L_2/L ratio for both interface shapes. In this regime, the increase in adhesion was found to be higher for the flat interface than for the hemispherical interface. This trend is reflected in the simulations. Optical microscopy of the interfaces showed that cracks were always initiated at the contact edges and propagated to cause fast delamination. Therefore, no differences between pull-off and crack initiation forces were observed.

3.2.2. *Regime of small soft layer thickness*

For soft layers with L_2/L ratios smaller than 0.06 (E_1/E_2=350) or than 0.03 (E_1/E_2=2), detachment occurred by a different mechanism and seemed to depend on interface shape. For flat interfaces (Fig. 6a), a drop in adhesion strength was observed. The detachment mechanism changed from single edge crack to several finger-like cracks which propagated radially towards the centre of the fibril; this detachment mechanism is reminiscent of earlier studies on thin soft films (Nase et al., 2008). By contrast, the fibrils with the hemispherical interface (Fig. 6b), showed a steady increase of the adhesion strength with decreasing L_2/L ratio. Here, a transition from edge to centre cracks could be observed. Interestingly, the primary crack did not cause fast detachment, but grew in a stable manner up to a critical diameter of more than half of the total diameter. Therefore, the pull-off forces were much larger than the crack initiation forces as is indicated by the arrows in Fig. 6b.

4. Discussion

A novel concept for designing bioinspired dry adhesives was introduced in this paper: comparatively stiff fibrils with a thin soft material layer on the terminal face. Numerical results demonstrated that such composite fibrils have reduced stress singularities at the contact edges, which typically control the detachment of flat punch fibrils from substrates (Akisanya and Fleck, 1997; Khaderi et al., 2015). Stronger adhesion is achieved by reducing the corner stresses; this is similar to the findings previously reported for mushroom fibrils, where the gradually widening terminal face results in a more uniform stress distribution and strongly enhanced

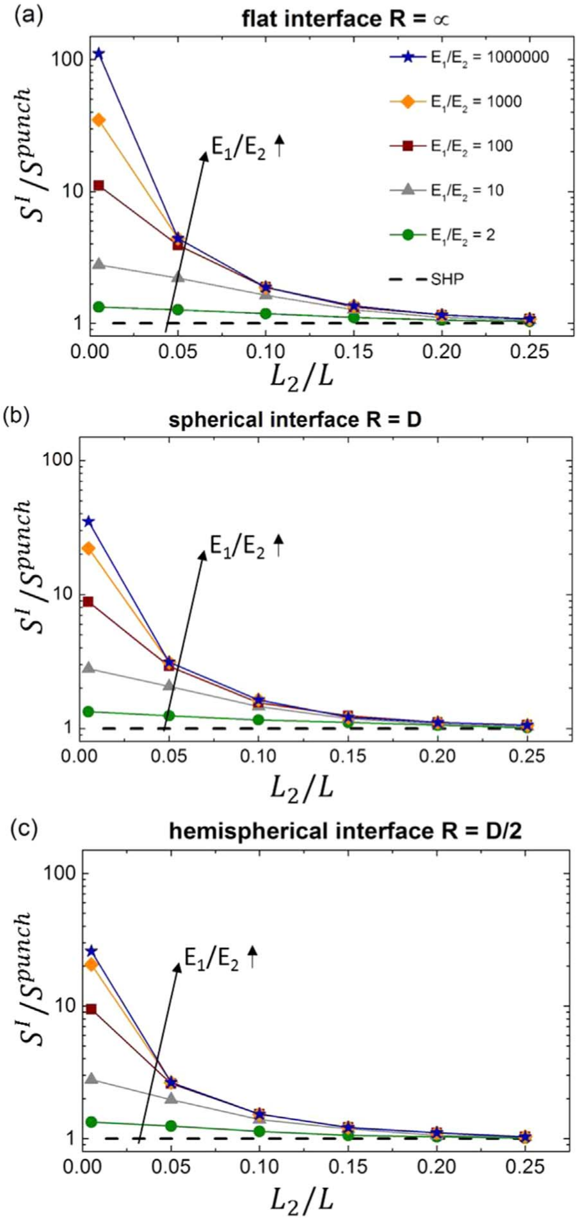

Fig. 5. Calculated influence of Young's modulus ratio on adhesive strength, normalized to that of a straight homogeneous punch (SHP), with the following interface shapes: (a) flat, (b) spherical ($R = D$), and (c) hemispherical ($R = D/2$). The different Young's modulus ratios are E_1/E_2=2 (green, circles), 10 (grey, triangles), 100 (red, squares), 1000 (orange, diamonds) and 1000000 (blue, stars). (For interpretation of the references to colour in this figure legend, the reader is referred to the web version of this article.)

adhesion (Balijepalli et al., 2016; del Campo et al., 2007; Heepe and Gorb, 2014). Our composite fibril design, by contrast, exhibits a uniform axial cross-sectional area with several possible advantages: fibrils without re-entrant corners are easier to fabricate and will be less prone to elastic collapse, which is known to counteract adhesion.

Our parametric study reveals a counter-intuitive trend: thinner soft layers (with smaller L_2/L) create substantially better adhesion. The reason is that, for all Young's modulus ratios, a smaller layer thickness results in a decreased corner stress while the stress at the centre is increased. Recently, a similar trend was found by Minsky and Turner (Minsky and Turner, 2015), who studied a different, but related fibril geometry. A stiff fibril stalk, when fully coated with a thin soft polymer layer, exhibited improved adhesion, based on a cohesive zone model. However their results were limited to only one elastic modulus ratio. In our work, the variation of that ratio also affects the tensile stress distribution along the fibril-substrate interface, with higher ratios leading to significantly better adhesion. However, when $L_2/L > 0.05$, the effect decreases for higher ratios and disappears for a Young's modulus ratio exceeding three orders of magnitude. Interestingly, the composite fibrils of ladybugs (Peisker et al., 2013) exhibit a modulus ratio of such a magnitude, and not more.

Table 2
Adhesion strength values for different interfaces which include flat interface (*FI*), spherical interface (*SI*) with radius $R = D$and hemispherical (*HSI*) for radius$R = D/2$, represented as adhesion of composite fibrils normalized by that of a straight homogeneous punch.

S^I/S^{punch}	E_1/E_2=2			E_1/E_2 = 10			E_1/E_2 = 100			E_1/E_2 = 1000			E_1/E_2 = 1000000		
L_2/L	*FI* R=∞	*SI* R=D	*HSI* R=$D/2$	*FI* R=∞	*SI* R=D	*HSI* R=$D/2$	*FI* R=∞	*SI* R=D	*HSI* R=$D/2$	*FI* R=∞	*SI* R=D	*HSI* R=$D/2$	*FI* R=∞	*SI* R=D	*HSI* R=$D/2$
0.25	1.03	1.01	1.01	1.06	1.03	1.03	1.08	1.06	1.06	1.06	1.06	1.03	1.06	1.06	1.03
0.2	1.06	1.06	1.03	1.11	1.08	1.06	1.16	1.11	1.11	1.16	1.11	1.11	1.16	1.11	1.11
0.15	1.11	1.11	1.06	1.27	1.19	1.19	1.33	1.24	1.21	1.36	1.21	1.21	1.36	1.21	1.21
0.1	1.19	1.16	1.13	1.64	1.46	1.39	1.88	1.56	1.53	1.88	1.64	1.53	1.88	1.64	1.53
0.05	1.27	1.24	1.24	2.21	2.06	1.97	3.93	2.91	2.59	4.41	3.12	2.65	4.41	3.12	2.65
0.005	1.33	1.33	1.33	2.78	2.78	2.78	11.07	8.79	9.42	44.06	22.08	20.61	44.06	35.00	25.94

The materials interface curvature strongly affected the tensile stress distribution along the fibril-substrate interface, particularly for very thin films. Out of the different interface shapes examined, the adhesion of a composite fibril with a flat interface shows the lowest maximum stress at the corner and the centre along the fibril-substrate interface. The simulations indicate that higher curvatures lead to higher stresses at the centre and the edge compared to the flat interface. However, the contribution of the materials interface curvature to the stress distribution disappears for $L_2/L \approx 0.25$.

It is instructive to examine more closely the correlation between our numerical results and the experimental measurements on single macroscopic composite fibrils. While the agreement is not perfect, the trend to higher normalized adhesion strength with decreasing layer thickness is also found in the experiments (Fig. 6). What is not found in the calculations is the drop in adhesion strength seen in the flat interface fibril for small L_2/L ratios. It is very likely that this is caused by an alternative detachment mechanism not considered in the model, i.e. finger-like crack growth starting from the edge as observed in Fig. 6a. Such behaviour is well known in interface mechanics as the Saffman–Taylor instability (Derks et al., 2003; Nase et al., 2011; Shull and Creton, 2004). Interestingly, the transition from single-edge crack propagation to delamination by instabilities depends on the stiffness of the stalk. In the case of the hemispherical interfaces, a drop of adhesion strength was not found in the experiments although a change in detachment mechanism initiated by centre cracks occurred (Fig. 6b). The mechanism change is in agreement with the numerical calculations, which predict a strong increase of the centre stresses when the soft layer becomes thinner. Why the presence of centre cracks still leads to increasing adhesion strengths is a matter of conjecture. A possible explanation lies in the steep decrease of the stress from the centre to the edges (see Fig. 4), which may induce stable

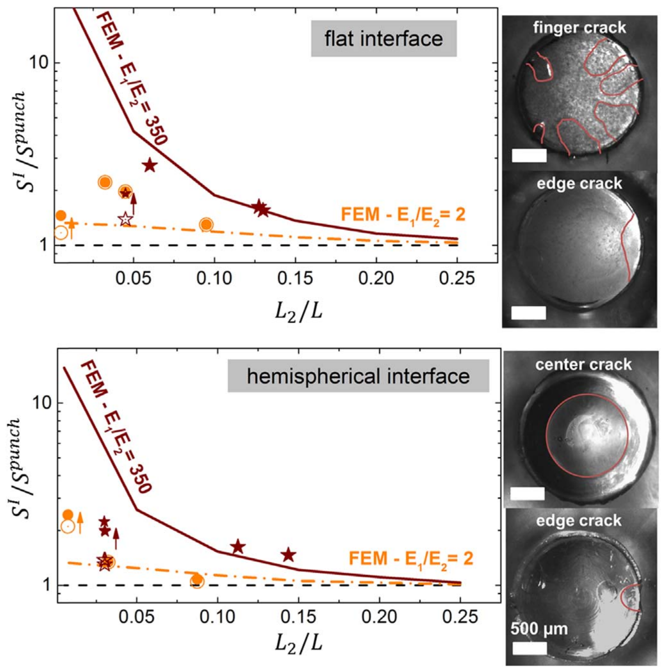

Fig. 6. Comparison of normalized adhesion strengths from experiments (symbols) and numerical calculations (lines) for composite fibrils with (a) flat interface and (b) hemispherical interface ($R = D/2$) for E_1/E_2=2 and 350. The lines refer to calculations for a SHP (black, dashed), and a composite fibril with E_1/E_2=2 (orange, dashes and dots) and 350 (red, solid). Light green circles represent experiments with E_1/E_2=2 and dark green stars with E_1/E_2=350. Filled symbols represent pull-off forces, empty symbols crack initiation forces. Arrows indicate the samples for which the two forces differ significantly. Optical micrographs represent the characteristic detachment mechanisms that were observed for (a) flat and (b) hemispherical interfaces depending on the soft layer thickness. The crack fronts are highlighted by red lines. (For interpretation of the references to colour in this figure legend, the reader is referred to the web version of this article.)

crack propagation. Incorporation of this additional mechanism into the numerical calculations would be possible (see, for instance, (Balijepalli et al., 2016)), but is beyond the scope of the present paper.

Overall, our research provides a promising alternative for straight homogeneous punch or mushroom-type fibrils. The combination of numerical calculations with model experiment has provided us with new insight for the optimization of micropatterned dry adhesive surfaces. The more benign stress distribution of the composite fibrils is reminiscent of the effect found in previous studies for mushroom fibrils while reducing the manufacturing complexity. Additionally, our geometry allows for the use of softer materials, as the stiffer stalk will stabilize the fibrils against collapse or clustering. A more detailed experimental study of such composite fibrils is currently underway (Fischer et al., 2016).

5. Conclusion

In this investigation, we demonstrated the potential of composite fibril structures that combine relatively stiff stalks with very soft tip layers. With this design, high aspect ratio structures with straight sidewalls can be manufactured without the risk of collapse of thin features. The soft material forming the tip of the microstructures provides a benign stress distribution and high adaptability to the substrate while the stiffer underlying material ensures mechanical stability. The following conclusions can be drawn:

- The adhesion of composite fibrillar structures can be tuned by varying the Young's moduli of the two material components, by manipulating the curvature of their interface, and by changing the soft layer thickness.
- Thinner soft layers (smaller L_2/L) are found to result in lower corner stresses and hence in higher adhesive strength provided that detachment is controlled by the corner singularity.

- Higher Young's modulus ratios (E_1/E_2) increase the adhesive strength.
- Flat interfaces lead to better adhesion than spherical and hemispherical interfaces for the case of edge crack detachment. For very thin soft layers, the experimentally observed detachment is different and depends on the interface curvature. Thus, detachment from the centre provoked by a curved interface may result in better adhesion.
- The experimental results can be explained reasonably well by the numerical simulations as long as detachment occurs by edge cracks. Below a limiting L_2/L ratio, a transition from edge to centre crack occurred in the experiments; these mechanisms are not yet part of the calculations.

Acknowledgements

S.C.L.F. would like to acknowledge the technical support by Martin Schmitz and Susanne Selzer. Furthermore, Lukas Engel is acknowledged for his help in manufacturing composite fibrils. E.A., R.H. and S.C.L.F. acknowledge funding from the European Research Council under the European Union/ERC Advanced Grant "Switch2Stick", Agreement no. 340929.

Appendix A. Analytical solution for corner singularity

The singular terms in the asymptotic normal stress (σ_{22}) and shear stress (σ_{12}) components are given by Eqs. (A1) and (A2):

$$\sigma_{22} = H_1 r^{-0.406} \tag{A1}$$

$$\sigma_{12} = 0.505 H_1 r^{-0.406} \tag{A2}$$

where r is the distance from the fibril edge, and the directions X_1 and X_2 are shown in Fig. 1. The amplitude term H_1 is dependent on the fibril diameter, the remote stress and a calibration coefficient $\tilde{a}$:

$$H_1 = \sigma_A D^{0.406} \tilde{a} \tag{A3}$$

The calibration coefficients of a straight homogeneous punch (SHP) are a_1=0.331 for the plane strain and a_1=0.278 for the axisymmetric case according to Khaderi et al. (2015). The asymptotic stress solutions for the plane strain case in logarithmic form are thus:

$$\log(\sigma_{22}/\sigma_A) = -0.480 - 0.406 \log(r/D) \quad \log(\sigma_{12}/\sigma_A) = -0.777 - 0.406 \log(r/D) \tag{A4}$$

and, for axial symmetry,

$$\log(\sigma_{22}/\sigma_A) = -0.556 - 0.406 \log(r/D) \quad \log(\sigma_{12}/\sigma_A) = -0.853 - 0.406 \log(r/D). \tag{A5}$$

The resulting normal and shear stress along the interface of a SHP and a rigid substrate for plane strain and axisymmetric fibrils are shown in Fig. C1 and in Appendix C. In order to predict the adhesive strength of the fibril, we assume a small detachment length l at its edge where the corner singularity controls the detachment behaviour. A detailed analysis was provided by Balijepalli et al. (2016).

The stress distribution near the crack tip can be described by

$$\sigma_{22} = \frac{K_I}{\sqrt{2\pi\zeta}} \text{ and } \sigma_{12} = \frac{K_{II}}{\sqrt{2\pi\zeta}} \tag{A6}$$

where ζ is the distance from the crack tip as shown in Fig. C2 in Appendix C. The Mode I and Mode II stress intensity factors, K_I and K_{II}, are given by

$$K_I{=}2.\ 6H_1 l^{0.094}{=}2.\ 6\sigma_A D^{0.406}\tilde{a}\, l^{0.094} \tag{A7}$$

and

$$K_{II}{=}0.\ 8H_1 l^{0.094}{=}0.\ 8\sigma_A D^{0.406}\tilde{a}\, l^{0.094} \tag{A8}$$

The energy release rate during detachment is given by

$$G = \frac{1-\nu^2}{2E_2}(K_I^2 + K_{II}^2) = \frac{3}{8E_2}(K_I^2 + K_{II}^2) = \frac{2.\ 8\sigma_A^2 D^{0.81} l^{0.19}\tilde{a}^2}{E_2} \tag{A9}$$

where E_2 is Young's modulus of the soft layer in contact with the rigid substrate and ν is the associated Poisson's ratio, equal to 0.5 consistent with incompressibility. For detachment to occur, the energy release rate must be equal to the adhesion energy, W. The adhesion strength of the composite fibril S^I can be expressed as

$$S^I = \frac{0.\ 6\sqrt{E_2 W}}{D^{0.406} l^{0.094}\tilde{a}} \tag{A10}$$

We define a normalized adhesion strength by dividing by the value for the straight homogeneous punch S^{punch}, which is assumed to have the same initial crack length:

$$\frac{S^I}{S^{punch}} = \frac{a_1}{\tilde{a}} \tag{A11}$$

Appendix B. Asymptotic analysis of the stress in a stiff adherent axisymmetric cylindrical fibril with a thin compliant layer at its tip

We consider a circular cylindrical fibril of diameter D adhering to a rigid flat substrate. The fibril is also rigid other than a thin layer of compliant material at the tip where the fibril adheres to the substrate. The geometry is axisymmetric. The compliant material is incompressible and linear elastic with shear modulus μ. The relevant equilibrium equations are

$$\begin{aligned}
&\tfrac{\partial\tilde{\sigma}_{rr}}{\partial\tilde{r}} + \tfrac{\tilde{\sigma}_{rr} - \tilde{\sigma}_{\theta\theta}}{\tilde{r}} + \tfrac{\partial\tilde{\sigma}_{rz}}{\partial\tilde{z}} = 0\\
&\tfrac{\partial\tilde{\sigma}_{rz}}{\partial\tilde{r}} + \tfrac{\tilde{\sigma}_{rz}}{\tilde{r}} + \tfrac{\partial\tilde{\sigma}_{zz}}{\partial\tilde{z}} = 0
\end{aligned} \tag{B1}$$

where the stress components are given in cylindrical polar coordinates and $\tilde{r}$, θ, $\tilde{z}$ are those cylindrical polar coordinates. The elasticity relationships are

$$\begin{aligned}
&\tfrac{\partial\tilde{u}_r}{\partial\tilde{r}} = \tfrac{1}{2\mu}(\tilde{\sigma}_{rr} + \tilde{p})\\
&\tfrac{\tilde{u}_r}{\tilde{r}} = \tfrac{1}{2\mu}(\tilde{\sigma}_{\theta\theta} + \tilde{p})\\
&\tfrac{\partial\tilde{u}_z}{\partial\tilde{z}} = \tfrac{1}{2\mu}(\tilde{\sigma}_{zz} + \tilde{p})\\
&\tfrac{\partial\tilde{u}_z}{\partial\tilde{r}} + \tfrac{\partial\tilde{u}_r}{\partial\tilde{z}} = \tfrac{\tilde{\sigma}_{rz}}{\mu}
\end{aligned} \tag{B2}$$

where $\tilde{u}_r$ and $\tilde{u}_z$ are the axial displacements and $\tilde{p} = -(\tilde{\sigma}_{rr} + \tilde{\sigma}_{\theta\theta} + \tilde{\sigma}_{zz})/3$ is the pressure, *i.e.* the negative of the hydrostatic stress. Incompressibility is embedded in Eq. (B2) but can also be stated as

$$\frac{\partial\tilde{u}_r}{\partial\tilde{r}} + \frac{\tilde{u}_r}{\tilde{r}} + \frac{\partial\tilde{u}_z}{\partial\tilde{z}} = 0 \tag{B3}$$

The boundary conditions are

$$\tilde{u}_r = \tilde{u}_z = 0 \text{ on } \tilde{z} = 0 \tag{B4}$$

and

$$\begin{matrix}\tilde{u}_r = 0\\ \tilde{u}_z = \Delta\end{matrix} \quad \text{on } \tilde{z} = \tilde{h}(\tilde{r}) \tag{B5}$$

where Δ is the upward displacement of the rigid segment of the fibril and $\tilde{z} = \tilde{h}(\tilde{r})$ is the interface between the complaint layer and the rigid segment of the fibril. We assume that $\tilde{h}(\tilde{r}) < < D$ so that the complaint layer is thin compared to the diameter of the fibril. The traction boundary conditions are

$$\tilde{\sigma}_{rr}\left(\frac{D}{2}, \tilde{z}\right) = 0 \text{ and } \tilde{\sigma}_{rz}\left(\frac{D}{2}, \tilde{z}\right) = 0 \tag{B6}$$

Now define the parameter η such that $\eta = \tilde{h}(D/2)$. It follows that $\eta << D$ and thus $\delta = 2\eta/D << 1$ is a small parameter. Now normalize lengths such that $\tilde{r} = Dr/2$, $\tilde{z} = \eta z$, and the displacements are such that $\tilde{u}_r = \Delta u_r$ and $\tilde{u}_z = \Delta u_z$. It follows that u_z, r and z are $O(1)$. We normalize the stresses by Σ, to be determined, such that $\tilde{\sigma}_{ij} = \Sigma\sigma_{ij}$. However, we specify that σ_{zz} is $O(1)$, so that Σ is the order of the stress applied to the fibril. As a result of the normalizations, the equations become as follows. For equilibrium we have

$$\begin{aligned} &\delta\frac{\partial\sigma_{rr}}{\partial r} + \delta\frac{\sigma_{rr}-\sigma_{\theta\theta}}{r} + \frac{\partial\sigma_{rz}}{\partial z} = 0 \\ &\delta\frac{\partial\sigma_{rz}}{\partial r} + \delta\frac{\sigma_{rz}}{r} + \frac{\partial\sigma_{zz}}{\partial z} = 0 \end{aligned} \tag{B7}$$

For elasticity we deduce that

$$\begin{aligned} &\frac{2\Delta\partial u_r}{D\partial r} = \frac{\Sigma}{2\mu}(\sigma_{rr} + p) \\ &\frac{2\Delta u_r}{Dr} = \frac{\Sigma}{2\mu}(\sigma_{\theta\theta} + p) \\ &\frac{\Delta\partial u_z}{\eta\partial z} = \frac{\Sigma}{2\mu}(\sigma_{zz} + p) \\ &\frac{2\Delta\partial u_z}{D\partial r} + \frac{\Delta\partial u_r}{\eta\partial z} = \frac{\Sigma\sigma_{rz}}{\mu} \end{aligned} \tag{B8}$$

where $\tilde{p} = \Sigma p$, incompressibility becomes

$$\delta\frac{\partial u_r}{\partial r} + \delta\frac{u_r}{r} + \frac{\partial u_z}{\partial z} = 0 \tag{B9}$$

and the boundary conditions are

$$u_r = u_z = 0 \text{ on } z = 0 \tag{B10}$$

$$u_r = 0 \text{ on } z = \tilde{h}(r)/\eta \tag{B11}$$

$$u_z = 1 \text{ on } z = \tilde{h}(r)/\eta \tag{B12}$$

and

$$\sigma_{rr}(1, z) = 0 \text{ and } \sigma_{rz}(1, z) = 0 \tag{B13}$$

From the set of equations above we deduce that to satisfy incompressibility u_r must be $O(1/\delta)$, i.e. much bigger than u_z. The first of Eq. (B7) shows that σ_{rz}/σ_{rr} is $O(\delta)$ and we assume that σ_{zz} and σ_{rr} are the same order of magnitude. Therefore σ_{rz} is $O(\delta)$. Inspection of the last of Eq. (B8) then allows us to deduce that $\Delta/\eta\delta$ and $\Sigma\delta/\mu$ are of the same order. Therefore, we write $\Sigma = \Delta\mu/\eta\delta^2$. As a consequence, Eq. (B8) becomes

$$\begin{aligned} &\delta^3\frac{\partial u_r}{\partial r} = \frac{1}{2}(\sigma_{rr} + p) \\ &\delta^3\frac{u_r}{r} = \frac{1}{2}(\sigma_{\theta\theta} + p) \\ &\delta^2\frac{\partial u_z}{\partial z} = \frac{1}{2}(\sigma_{zz} + p) \\ &\delta^3\frac{\partial u_z}{\partial r} + \delta^2\frac{\partial u_r}{\partial z} = \sigma_{rz} \end{aligned} \tag{B14}$$

This immediately tells us that the deviatoric stresses are no greater than $O(\delta)$. Therefore, we deduce that we can expand the stresses asymptotically as

$$\begin{aligned} &p = p^{(0)} + \delta p^{(1)} + O(\delta^2) \\ &\sigma_{rr} = -p^{(0)} - \delta p^{(1)} + \delta^2\sigma_{rr}^{(2)} + O(\delta^3) \\ &\sigma_{\theta\theta} = -p^{(0)} - \delta p^{(1)} + \delta^2\sigma_{\theta\theta}^{(2)} + O(\delta^3) \\ &\sigma_{zz} = -p^{(0)} - \delta p^{(1)} + \delta^2\sigma_{zz}^{(2)} + O(\delta^3) \\ &\sigma_{rz} = \delta\sigma_{rz}{}^{(1)} + O(\delta^2) \end{aligned} \tag{B15}$$

where the terms with the parenthetical superscripts are $O(1)$. We have therefore assumed that the stresses are hydrostatic to leading order and that deviatoric stress terms are $O(\delta)$. To validate that assumption, we performed numerical simulations for a composite fibril with a flat interface and $L_2/L = 0.005$, $E_1/E_2 = 10^6$ and a Poisson's ratio of 0.49999 for both materials. The result obtained demonstrates that the stress in the thin layer is almost hydrostatic with a very small shear stress superimposed (not shown). This means that the applied load in the thin layer is supported to leading order by the hydrostatic stress, arising because of the incompressibility of the material. Similarly, we expand the displacements as

$$u_r = \frac{1}{\delta}u_r^{(-1)} + u_r^{(o)} + O(\delta)$$
$$u_z = u_r^{(o)} + \delta u_r^{(1)} + O(\delta^2) \tag{B16}$$

which is consistent with our deductions above.

We substitute Eq. (B15) into Eq. (B7) and obtain to leading order for equilibrium

$$-\frac{\partial p^{(0)}}{\partial r} + \frac{\partial \sigma^{(1)}{}_{rz}}{\partial z} = 0$$
$$-\frac{\partial p^{(0)}}{\partial z} = 0 \tag{B17}$$

The stress strain relationships to leading order become

$$\frac{\partial u_r^{(-1)}}{\partial r} = \frac{1}{2}(\sigma_{rr}^{(2)} + p^{(2)})$$
$$\frac{u_r^{(-1)}}{r} = \frac{1}{2}(\sigma_{\theta\theta}^{(2)} + p^{(2)})$$
$$\frac{\partial u_z^{(0)}}{\partial z} = \frac{1}{2}(\sigma_{rr}^{(2)} + p^{(2)})$$
$$\frac{\partial u_r^{(-1)}}{\partial z} = \sigma_{rz}^{(1)} \tag{B18}$$

Incompressibility to leading order is then

$$\frac{\partial u_r^{(-1)}}{\partial r} + \frac{u_r^{(-1)}}{r} + \frac{\partial u_z^{(0)}}{\partial z} = 0 \tag{B19}$$

Since there is no equation in which $p^{(1)}$ appears, we conclude it must be zero.

We now proceed to solve the Eqs., (B17–B19). The 2^{nd} of Eq. (B17) tells us that $p^{(0)}$ is independent of z and thus

$$p^{(0)} = p^{(0)}(r) \tag{B20}$$

The 1^{st} of Eq. (B17) thus gives us

$$\frac{\partial \sigma^{(1)}{}_{rz}}{\partial z} = \frac{dp^{(0)}(r)}{dr} \tag{B21}$$

which can be integrated to give

$$\sigma^{(1)}{}_{rz} = \tau(r) + z\frac{dp^{(0)}(r)}{dr} \tag{B22}$$

where $\tau(r)$ is the as yet unknown value of the normalized shear stress at the interface with the substrate. The result from Eq. (B22) may be inserted into the 4^{th} of Eq. (B18) to give

$$\frac{\partial u_r^{(-1)}}{\partial z} = \tau(r) + z\frac{dp^{(0)}(r)}{dr} \tag{B23}$$

This integrates to give

$$u_r^{(-1)} = z\tau(r) + \frac{1}{2}z^2\frac{dp^{(0)}(r)}{dr} \tag{B24}$$

where the boundary condition Eq. (B10) has been used. The boundary condition Eq. (B11) gives us from Eq. (B24)

$$h(r)\tau(r) + \frac{1}{2}h^2(r)\frac{dp^{(0)}(r)}{dr} = 0 \tag{B25}$$

where $h(r) = \tilde{h}/\eta$. We use Eq. (B25) to eliminate $\tau(r)$ in favour of $dp^{(0)}(r)/dr$ and then incompressibility in the form of Eq. (B19), with results from Eq. (B25) inserted, to give

$$-z\frac{1}{2}\frac{d}{dr}\left[h(r)\frac{dp^{(0)}(r)}{dr}\right] - \frac{1}{2}zh(r)\frac{dp^{(0)}(r)}{rdr} + \frac{1}{2}z^2\frac{d^2p^{(0)}(r)}{dr^2} + \frac{1}{2}z^2\frac{dp^{(0)}(r)}{rdr} + \frac{\partial u_z^{(0)}}{\partial z} = 0 \tag{B26}$$

We then integrate this to obtain

$$u_z^{(0)} = \frac{1}{4}z^2\frac{d}{dr}\left[h(r)\frac{dp^{(0)}(r)}{dr}\right] + \frac{1}{4}z^2h(r)\frac{dp^{(0)}(r)}{rdr} - \frac{1}{6}z^3\frac{d^2p^{(0)}(r)}{dr^2} - \frac{1}{6}z^3\frac{dp^{(0)}(r)}{rdr} \tag{B27}$$

where we have used the boundary condition Eq. (B10) at $z = 0$. Now use Eq. (B12) and we deduce that this leads to

$$\frac{d}{dr}\left[rh^3(r)\frac{dp^{(0)}(r)}{dr}\right] = 12r \tag{B28}$$

We integrate this once and obtain

$$\frac{dp^{(0)}(r)}{dr} = \frac{6r^2 + c_1}{rh^3(r)} \tag{B29}$$

where c_1 is a constant. We confine ourselves to cases where $h(0)$ is finite, and conclude that this leads to $c_1 = 0$, since otherwise the gradient of $p^{(0)}$ diverges. As a consequence, integration of B 29 gives us

$$p^{(0)} = 6\int_1^r \frac{\xi d\xi}{h^3(\xi)} \tag{B30}$$

where we have used the 1st of the boundary conditions in Eq. (B13) as it gives $p^{(0)}(1) = 0$.

Examples:

(1) Layer of uniform thickness.

In this case $h(r) = 1$ and Eq. (B30) becomes

$$p^{(0)}(r) = 3(r^2 - 1) \tag{B31}$$

which, through Eq. (B21) leads to

$$\sigma^{(1)}{}_{rz} = 3r(2z - 1) \tag{B32}$$

Therefore, we have all the leading order stresses since

$$\sigma_{rr}^{(0)} = \sigma_{\theta\theta}^{(0)} = \sigma_{zz}^{(0)} = -p^{(0)} = 3(1 - r^2) \tag{B33}$$

The tensile stresses are therefore greatest at the centre of the fibril. Note that the shear stress in Eq. (B32) is not zero at $r = 1$, violating the 2^{nd} boundary in Eq. (B13). However, the boundary condition is satisfied in an average sense since the integral of Eq. (B32) with respect to z from zero to 1 is zero. Since the shear stresses are lower order, this discrepancy is not significant. It would have to be fixed by a boundary layer, which the St. Venant principle shows would only affect the solution over a radial distance comparable to the thickness of the layer.

The results in Eqs. (B32 and B33) are normalized. We obtain the physical results by restoring the factors by which normalization took place. This gives

$$\begin{aligned}\tilde{\sigma}_{rr} = \tilde{\sigma}_{\theta\theta} = \tilde{\sigma}_{zz} = 3\Sigma(1 - r^2) = \tfrac{3\Delta\mu D^2}{4h^3}\left(1 - \tfrac{4\tilde{r}^2}{D^2}\right)\\ \tilde{\sigma}_{rz} = 3\Sigma\delta r(2z - 1) = \tfrac{3\Delta\mu\tilde{r}}{h^2}(\tfrac{2\tilde{z}}{h} - 1)\end{aligned} \tag{B34}$$

where h is the thickness of the compliant layer. It can be seen that the shear stress is much smaller than the direct stresses. The error in all stresses is small compared to the magnitude of the shear stress.

As a result of Eq. (B34) the highest tensile stress on the interface is $3\Delta\mu D^2/(4\eta^3) = E\Delta D^2/(4\eta^3)$, where E is Young's modulus. This is the stress at the centre of the fibril that will cause detachment if failure at the corner singularity is suppressed. Note that the solution in Eq. (B34) gives no information about the corner singularity as it represents a boundary layer at the edge of the fibril. We note that the maximum tensile stress at the interface is twice as high as the average stress on the interface.

(2) Layer with quadratic shape

This case can represent the rigid segment of the fibril having a circular shape where, following Hertz, we approximate these shapes by recognizing that the layer thickness is smaller than the diameters of the circle. However, the slope of the circular interface must remain small throughout its extent for the asymptotic analysis to be valid. This rules out the caser of $R = D/2$, though the case of $R = D$ may be admissible (see Fig. 1).

The shape of the thin layer is

$$h(r) = h_o + (1 - h_o)r^2 \tag{B35}$$

where $h_o = \eta_o/\eta$ with $\tilde{h}(0) = \eta_o$ and therefore is the narrowest segment of the thin layer.

Integration of Eq. (B30) then gives us

$$p^{(0)} = \frac{1}{4(1 - h_o)}\left\{1 - \frac{1}{[h_o + (1 - h_o)r^2]^2}\right\} \tag{B36}$$

and then

$$\sigma_{rz}^{(1)} = \frac{3r(2z - 1)}{[h_o + (1 - h_o)r^2]^3} \tag{B37}$$

These normalized can be converted to physical values by multiplication by the appropriate factors as was carried out to obtain Eq. (B34). Details will not be pursued. In this case, the maximum stress, which is at $\tilde{r} = 0$, is $(1 + h_o)/h_o = 1 + \tilde{h}(D/2)/\tilde{h}(0)$ times the average stress on the interface. We note that this result is valid for the flat interface, and predicts that the maximum stress rises above twice the average stress when the interface is circular, consistent with the results in Fig. 4.

Appendix C. Plane strain and Axisymmetric results

See Figs. C1-C9 and Tables C1-C3.

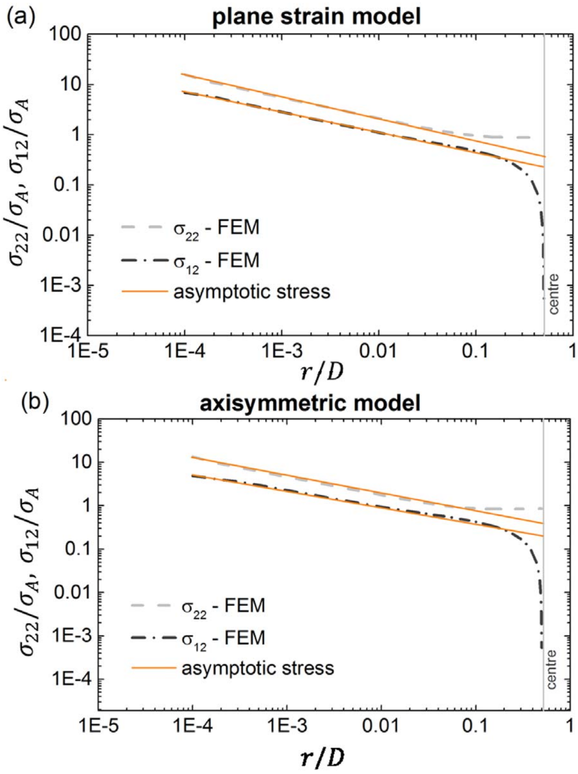

Fig. C1. Normalized normal (σ_{22}; light grey, dashed line) and shear (σ_{12}; dark grey, dashes and dots) tractions for the straight homogeneous punch (SHP) (corner to centre) for (a) plane strain and (b) axisymmetric cases. The remote applied stress is denoted by σ_A. The orange solid lines show linear fits of the two stress curves at the edge of the fibril.

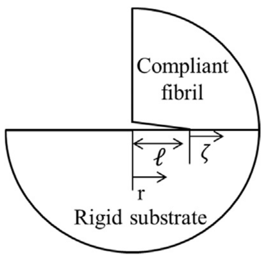

Fig. C2. Schematic of a small crack emanating along the interface from the corner of the contact.

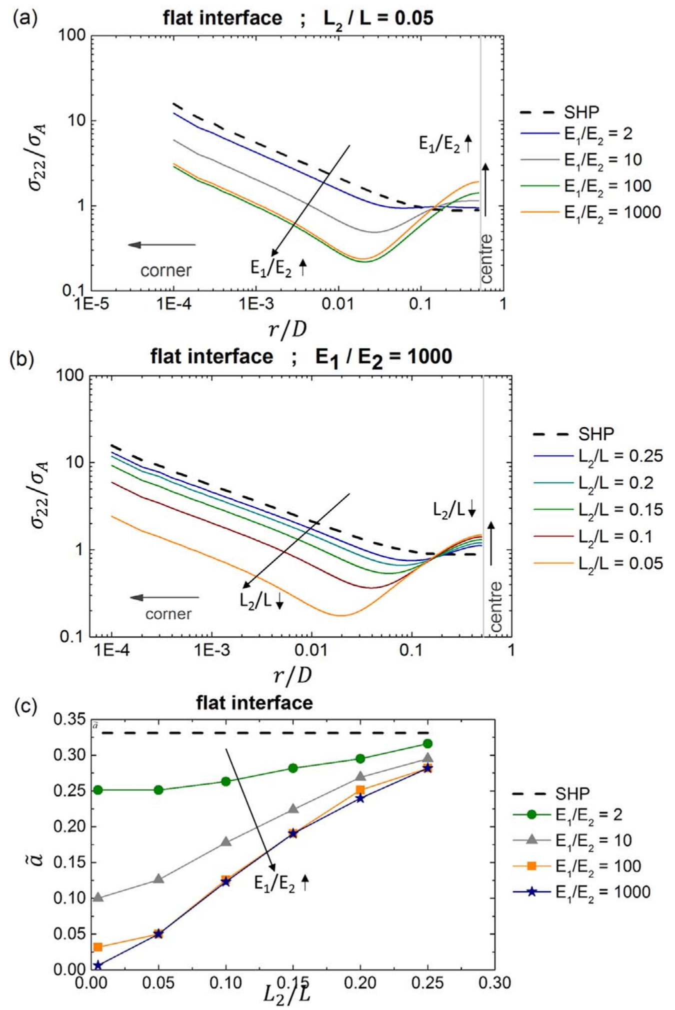

Fig. C3. Analysis of a composite fibril with a flat interface for plane strain. Tensile stress σ_{22}along the fibril and substrate interface for different combinations of (a) Young's modulus ratio $E_1/E_2$of the top and bottom part of the fibril respectively for a constant L_2/L = 0.05, and (b) height of the soft portion L_2 normalized by total height L and constant E_1/E_2=1000. (c) Calibration coefficient for composite fibrils for different combinations of the ratio of height L_2/L and Young's modulus E_1/E_2. The dashed black lines represent the straight homogeneous punch (SHP) results. The colours and symbol shapes reflect the varying parameters E_1/E_2 and L_2/L.

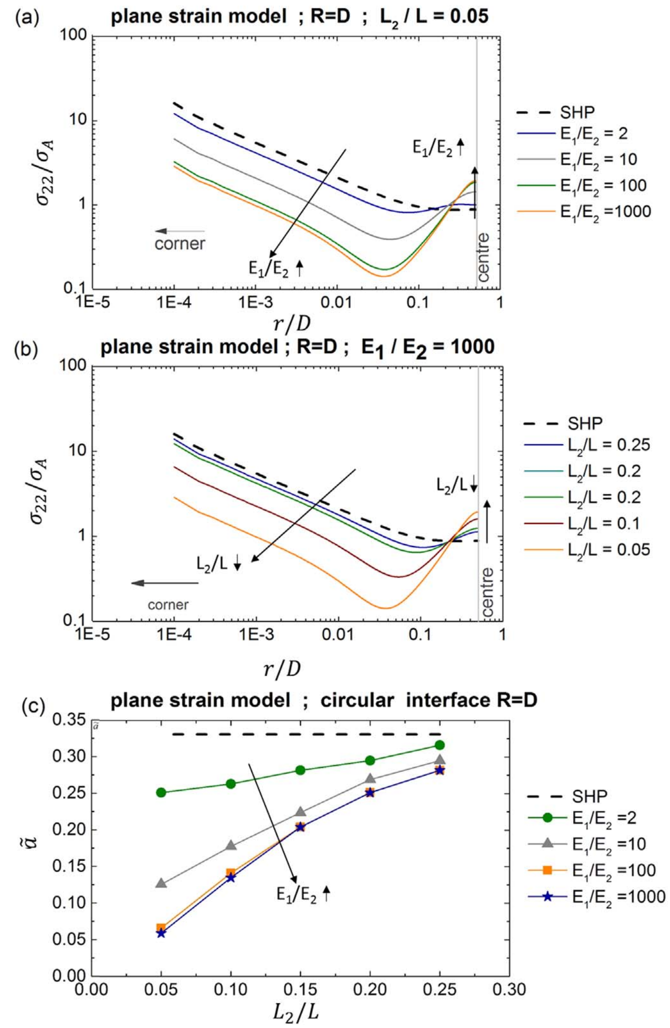

Fig. C4. Tensile stress σ_{22}along the fibril and substrate interface for a composite fibril with a circular interface ($R = D$) for different combinations of Young's modulus ratio $E_1/E_2$and layer thickness ratio L_2/L. The results are reported for the plane strain case. The dashed black lines represent the straight homogeneous punch (SHP) results. The colours and symbol shapes reflect the varying parameters E_1/E_2 and L_2/L.

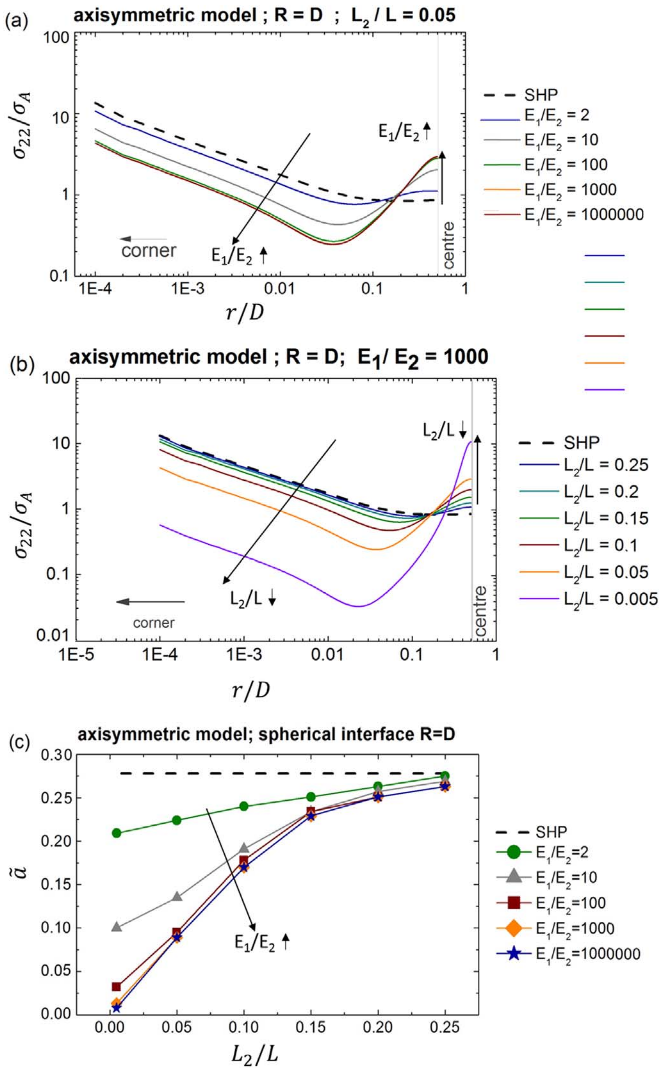

Fig. C5. Tensile stress σ_{22}along the fibril and substrate interface for a composite fibril with a spherical interface (R = D) for different combinations of Young's modulus ratio $E_1/E_2$and layer thickness ratio L_2/L. The results are reported for the axisymmetric case. The dashed black lines represent the straight homogeneous punch (SHP) results. The colours and symbol shapes reflect the varying parameters E_1/E_2 and L_2/L.

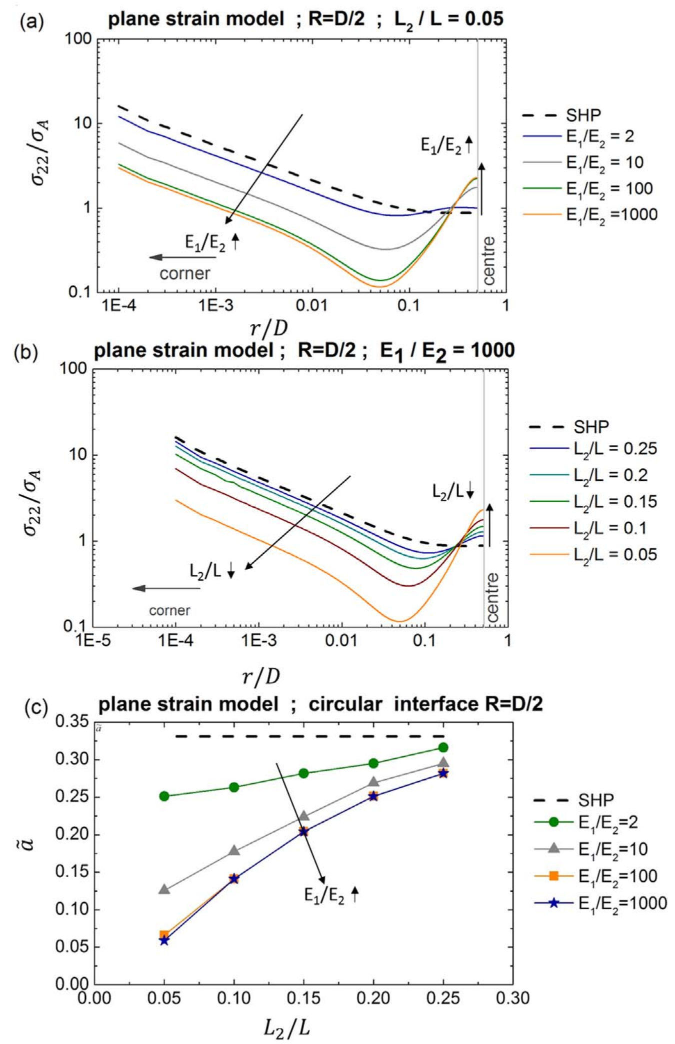

Fig. C6. Tensile stress σ_{22}along the fibril and substrate interface for a composite fibril with a circular interface (R = D/2) for different combinations of Young's modulus ratio E_1/E_2, layer thickness ratio L_2/L and the corresponding calibration coefficients. The results are reported for the plane strain case. The dashed black lines represent the straight homogeneous punch (SHP) results. The colours and symbol shapes reflect the varying parameters E_1/E_2 and L_2/L.

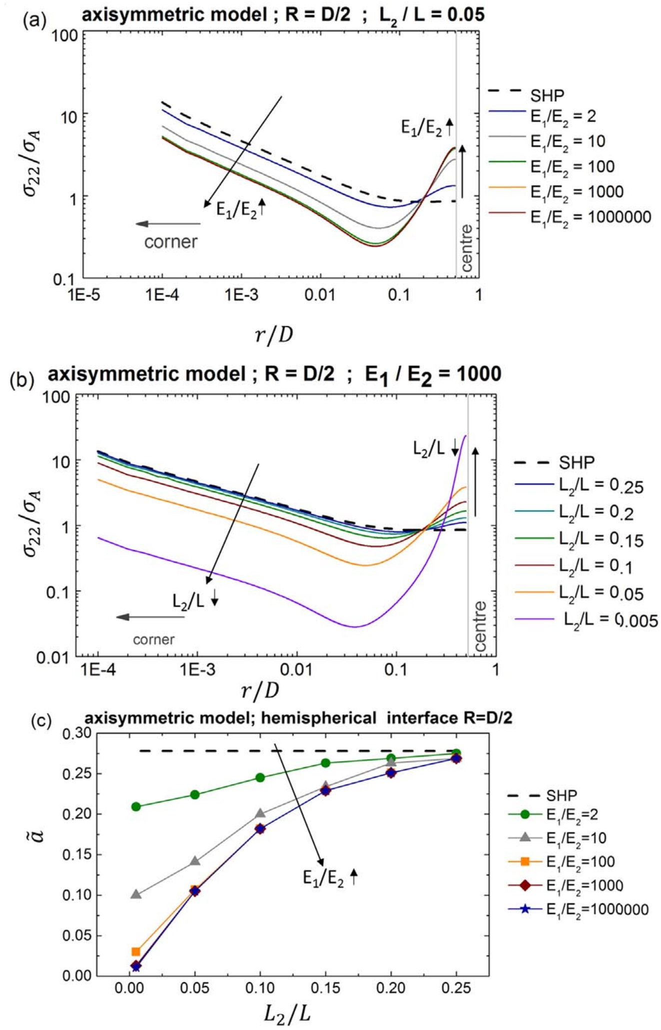

Fig. C7. Tensile stress σ_{22}along the fibril and substrate interface for a composite fibril with a hemispherical interface ($R = D/2$) for different combinations of Young's modulus ratio E_1/E_2, layer thickness ratio L_2/L and the corresponding calibration coefficients. The results are reported for the axisymmetric case. The dashed black lines represent the straight homogeneous punch (SHP) results. The colours and symbol shapes reflect the varying parameters E_1/E_2 and L_2/L.

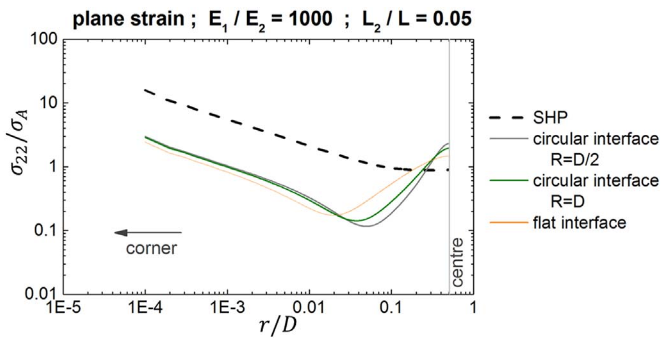

Fig. C8. Normal stress σ_{22}along the fibril and substrate interface for fibrils with different interface shapes and with L_2/L ratio 0.05 for the plane strain case. The dashed black lines represent the straight homogeneous punch (SHP) results.

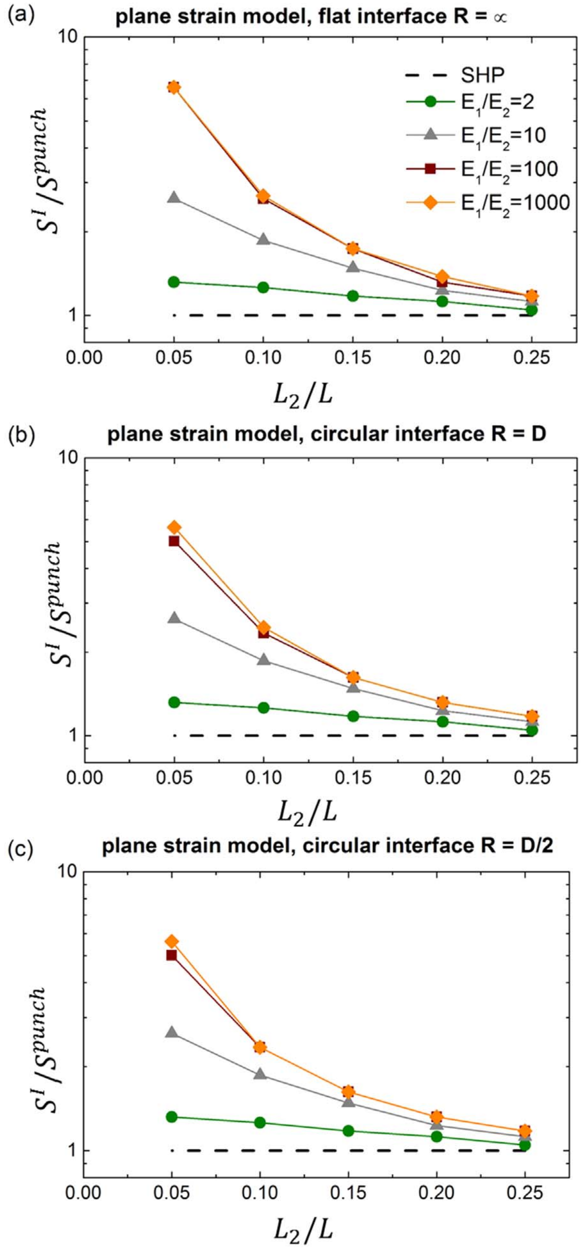

Fig. C9. Adhesion strength values for composite fibrils for different interfaces, and different combinations of height ratio L_2/L and Young's modulus E_1/E_2. The results are shown for a composite fibril with flat (a) and circular interface (b) where the radius R is equal to the diameter $D$of the fibril and (c) the radius R is equal to half of the diameter. The dashed black lines represent the straight homogeneous punch (SHP) results. The different Young's moduli compared are E_1/E_2= 2 (green, circles), 10 (grey, triangles), 100 (wine red, squares) and 1000 (orange, diamonds).

Table C1
Calibration coefficients $\tilde{\alpha}$ for a flat interface for the plane strain case.

L_2/L	$\tilde{\alpha}$			
	$E_1/E_2=2$	$E_1/E_2=10$	$E_1/E_2=100$	$E_1/E_2=1000$
0.25	0.316	0.295	0.282	0.282
0.2	0.295	0.269	0.251	0.240
0.15	0.281	0.224	0.190	0.190
0.1	0.263	0.178	0.126	0.123
0.05	0.251	0.126	0.050	0.050
0.005	0.251	0.1	0.032	0.006

Table C2
Calibration coefficients $\tilde{\alpha}$ for (a) circular (plane strain) and (b) spherical interface with radius $R = D$(axisymmetric) and hemispherical for radius $R = D/2$ (axisymmetric).

(a)

L_2/L	$\tilde{\alpha}$							
	$E_1/E_2=2$		$E_1/E_2=10$		$E_1/E_2=100$		$E_1/E_2=1000$	
	$R=D$	$R=D/2$	$R=D$	$R=D/2$	$R=D$	$R=D/2$	$R=D$	$R=D/2$
0.25	0.316	0.316	0.295	0.295	0.282	0.282	0.282	0.282
0.2	0.295	0.295	0.269	0.269	0.251	0.251	0.251	0.251
0.15	0.282	0.282	0.224	0.224	0.204	0.204	0.204	0.204
0.1	0.263	0.263	0.178	0.178	0.141	0.141	0.135	0.141
0.05	0.251	0.251	0.126	0.126	0.066	0.066	0.059	0.059

(b)

L_2/L	$\tilde{\alpha}$									
	$E_1/E_2=2$		$E_1/E_2=10$		$E_1/E_2=100$		$E_1/E_2=1000$		$E_1/E_2=1000000$	
	$R=D$	$R=D/2$	$R=D$	$R=D/2$	$R=D$	$R=D/2$	$R=D$	$R=D/2$	$R=D$	$R=D/2$
0.25	0.275	0.275	0.269	0.269	0.263	0.263	0.263	0.269	0.263	0.269
0.2	0.263	0.269	0.257	0.263	0.251	0.251	0.251	0.251	0.251	0.251
0.15	0.251	0.263	0.234	0.234	0.224	0.229	0.229	0.229	0.229	0.229
0.1	0.240	0.245	0.191	0.200	0.178	0.182	0.170	0.182	0.170	0.182
0.05	0.224	0.224	0.135	0.141	0.095	0.107	0.089	0.105	0.089	0.105
0.005	0.209	0.209	0.100	0.100	0.032	0.030	0.013	0.013	0.008	0.011

Table C3
Adhesion strength S^I/S^{punch} for the flat interface (FI) and circular interfaces (CI) $R = D$ and $R = D/2$ for the plane strain case.

S^I/S^{punch}	$E_1/E_2=2$			$E_1/E_2=10$			$E_1/E_2=100$			$E_1/E_2=1000$		
	FI	CI		FI	CI		FI	CI		FI	CI	
L_2/L	$R=\infty$	$R=D$	$R=D/2$	$R=\infty$	$R=D$	$R=D/2$	$R=\infty$	$R=D$	$R=D/2$	$R=\infty$	$R=D$	$R=D/2$
0.25	1.05	1.05	1.05	1.12	1.12	1.12	1.17	1.17	1.17	1.17	1.17	1.17
0.2	1.12	1.12	1.12	1.23	1.23	1.23	1.32	1.32	1.32	1.32	1.32	1.32
0.15	1.17	1.17	1.17	1.48	1.48	1.48	1.74	1.62	1.62	1.74	1.62	1.62
0.1	1.26	1.26	1.26	1.86	1.86	1.86	2.63	2.34	2.34	2.63	2.45	2.34
0.05	1.32	1.32	1.32	2.63	2.63	2.63	6.61	5.01	5.01	6.61	5.62	5.62

References

Abaqus6.11, 2011. Documentation. Dassault Systems, Simulia Corporation, Providence, Rhode Island, USA.
Akisanya, A.R., Fleck, N.A., 1997. Interfacial cracking from the freeedge of a long bi-material strip. Int. J. Solids Struct. 34, 1645–1665.
Aksak, B., Sahin, K., Sitti, M., 2014. The optimal shape of elastomer mushroom-like fibers for high and robust adhesion. Beilstein J. Nanotechnol. 5, 630–638.
Arzt, E., Enders, S., Gorb, S., 2002. Towards a micromechanical understanding of biological surface devices. Z. Metall. 93, 345–351.
Arzt, E., Gorb, S., Spolenak, R., 2003. From micro to nano contacts in biological attachment devices. Proc. Natl. Acad. Sci. USA 100, 10603–10606.
Autumn, K., Liang, Y.A., Hsieh, S.T., Zesch, W., Chan, W.P., Kenny, T.W., Fearing, R., Full, R.J., 2000. Adhesive force of a single gecko foot-hair. Nature 405, 681–685.
Autumn, K., Sitti, M., Liang, Y.A., Peattie, A.M., Hansen, W.R., Sponberg, S., Kenny, T.W., Fearing, R., Israelachvili, J.N., Full, R.J., 2002. Evidence for van der Waals adhesion in gecko setae. Proc. Natl. Acad. Sci. USA 99, 12252–12256.
Bae, W.G., Kim, D., Kwak, M.K., Ha, L., Kang, S.M., Suh, K.Y., 2013b. Enhanced Skin adhesive patch with modulus-tunable composite micropillars. Adv. Healthc. Mater. 2, 109–113.
Bae, W.-G., Kwak, M.K., Jeong, H.E., Pang, C., Jeong, H., Suh, K.-Y., 2013a. Fabrication and analysis of enforced dry adhesives with core-shell micropillars. Soft Matter 9, 1422–1427.
Balijepalli, R.G., Begley, M.R., Fleck, N.A., McMeeking, R.M., Arzt, E., 2016. Numerical simulation of the edge stress singularity and the adhesion strength for compliant mushroom fibrils adhered to rigid substrates. Int. J. Solids Struct. 85–86, 160–171.
Barreau, V., Hensel, R., Guimard, N.K., Ghatak, A., McMeeking, R.M., Arzt, E., 2016. Fibrillar elastomeric micropatterns create tunable adhesion even to rough surfaces. Adv. Funct. Mater. 26, 4687–4694.
Boesel, L.F., Greiner, C., Arzt, E., del Campo, A., 2010. Gecko-inspired surfaces: a path to strong and reversible dry adhesives. Adv. Mater. 22, 2125–2137.
del Campo, A., Arzt, E., 2007. Design parameters and current fabrication approaches for developing bioinspired dry adhesives. Macromol. Biosci. 7, 118–127.
del Campo, A., Arzt, E., 2011. Generating Micro- and Nanopatterns on Polymeric Materials. John Wiley & Sons, ISBN: 978-3-527-32508-5.
del Campo, A., Greiner, C., Arzt, E., 2007. Contact shape controls adhesion of bioinspired fibrillar surfaces. Langmuir 23, 10235–10243.
Carbone, G., Pierro, E., 2012. Sticky bio-inspired micropillars: finding the best shape. Small 8, 1449–1454.
Derks, D., Lindner, A., Creton, C., Bonn, D., 2003. Cohesive failure of thin layers of soft model adhesives under tension. J. Appl. Phys. 93, 1557–1566.
Fischer, S.C.L., Levy, O., Kroner, E., Hensel, R., Karp, J.M., Arzt, E., 2016. Bioinspired polydimethylsiloxane-based composites with high shear resistance against wet tissue. J. Mech. Behav. Biomed. Mater..
Gao, H., Yao, H., 2004. Shape insensitive optimal adhesion of nanoscale fibrillar structures. Proc. Natl. Acad. Sci. USA 101, 7851–7856.
Gao, H., Wang, X., Yao, H., Gorb, S., Arzt, E., 2005. Mechanics of hierarchical adhesion structures of geckos. Mech. Mater. 37, 275–285.
Gorb, S., 2007. Attachment Devices of Insect Cuticle. Springer, Netherlands.
Gorb, S., Varenberg, M., Peressadko, A., Tuma, J., 2007. Biomimetic mushroom-shaped fibrillar adhesive microstructure. J. R. Soc. Interface 4, 271–275.
Gorb, S.N., 2008. Biological attachment devices: exploring nature's diversity for biomimetics. Philos. Trans. R. Soc. a-Math. Phys. Eng. Sci. 366, 1557–1574.
Gorb, S.N., Filippov, A.E., 2014. Fibrillar adhesion with no clusterisation: functional significance of material gradient along adhesive setae of insects. Beilstein J. Nanotechnol. 5, 837–845.
Greiner, C., del Campo, A., Arzt, E., 2007. Adhesion of bioinspired micropatterned surfaces: effects of pillar radius, aspect ratio, and preload. Langmuir 23, 3495–3502.
Greiner, C., Buhl, S., del Campo, A., Arzt, E., 2009. Experimental parameters controlling adhesion of biomimetic fibrillar surfaces. J. Adhes. 85, 646–661.
Heepe, L., Gorb, S.N., 2014. Biologically inspired mushroom-shaped adhesive microstructures. Annu. Rev. Mater. Res. 44, 173–203.
Huber, G., Gorb, S.N., Spolenak, R., Arzt, E., 2005. Resolving the nanoscale adhesion of individual gecko spatulae by atomic force microscopy. Biol. Lett. 1, 2–4.
Kamperman, M., Kroner, E., del Campo, A., McMeeking, R.M., Arzt, E., 2010. Functional adhesive surfaces with “Gecko” effect: the concept of contact splitting. Adv. Eng. Mater. 12, 335–348.
Khaderi, S.N., Fleck, N.A., Arzt, E., McMeeking, R.M., 2015. Detachment of an adhered micropillar from a dissimilar substrate. J. Mech. Phys. Solids 75, 159–183.
Kim, S., Sitti, M., 2006. Biologically inspired polymer microfibers with spatulate tips as repeatable fibrillar adhesives. Appl. Phys. Lett. 89, 261911–261913.
Kroner, E., Blau, J., Arzt, E., 2012a. Note: an adhesion measurement setup for bioinspired fibrillar surfaces using flat probes. Rev. Sci. Instrum., 83.
Kroner, E., Kaiser, J.S., Fischer, S.C.L., Arzt, E., 2012b. Bioinspired polymeric surface patterns for medical applications. J. Appl Biomater. Funct. Mater. 10, 287–292.
Kwak, M.K., Jeong, H.-E., Suh, K.Y., 2011. Rational design and enhanced biocompatibility of a dry adhesive medical skin patch. Adv. Mater. 23, 3949–3953.
Liu, J., Hui, C.Y., Jagota, A., Shen, L., 2009. A model for static friction in a film-terminated microfibril array. J. Appl. Phys. 106, 053520.
Mengüç, Y., Yang, S.Y., Kim, S., Rogers, J.A., Sitti, M., 2012. Gecko-inspired COntrollable Adhesive Structures Applied to Micromanipulation. Adv. Funct. Mater. 22, 1246–1254.
Menon, C., Murphy, M., Sitti, M., 2004. Gecko inspired surface climbing robots. In: Proceedings of the IEEE International Conference on Robotics and Biomimetics. ROBIO 2004, pp. 431–436.
Minsky, H.K., Turner, K.T., 2015. Achieving enhanced and tunable adhesion via composite posts. Appl. Phys. Lett. 106, 201604.
Murphy, M.P., Aksak, B., Sitti, M., 2009. Gecko-inspired directional and controllable adhesion. Small 5, 170–175.
Nase, J., Lindner, A., Creton, C., 2008. Pattern formation during deformation of a confined viscoelastic layer: from a viscous liquid to a soft elastic solid. Phys. Rev. Lett. 101, 074503.
Nase, J., Derks, D., Lindner, A., 2011. Dynamic evolution of fingering patterns in a lifted Hele–Shaw cell. Phys. Fluids 23, 123101.
Paretkar, D., Kamperman, M., Schneider, A.S., Martina, D., Creton, C., Arzt, E., 2011. Bioinspired pressure actuated adhesive system. Mater. Sci. Eng.: C 31, 1152–1159.
Peisker, H., Michels, J., Gorb, S.N., 2013. Evidence for a material gradient in the adhesive tarsal setae of the ladybird beetle Coccinella septempunctata. Nat. Commun. 4, 1661.
Purtov, J., Frensemeier, M., Kroner, E., 2015. Switchable adhesion in vacuum using bio-inspired dry adhesives. ACS Appl. Mater. Interfaces 7, 24127–24135.
Sathya, C., John, T., Kimberly, T., 2013. A microfabricated gecko-inspired controllable and reusable dry adhesive. Smart Mater. Struct. 22, 025013.
Scholz, I., Baumgartner, W., Federle, W., 2008. Micromechanics of smooth adhesive organs in stick insects: pads are mechanically anisotropic and softer towards the adhesive surface. J. Comp. Physiol. A 194, 373–384.
Shull, K.R., Creton, C., 2004. Deformation behavior of thin, compliant layers under tensile loading conditions. J. Polym. Sci. Part B: Polym. Phys. 42, 4023–4043.
Spolenak, R., Gorb, S., Arzt, E., 2005. Adhesion design maps for bio-inspired attachment systems. Acta Biomater. 1, 5–13.
Spuskanyuk, A.V., McMeeking, R.M., Deshpande, V.S., Arzt, E., 2008. The effect of shape on the adhesion of fibrillar surfaces. Acta Biomater. 4, 1669–1676.
Vajpayee, S., Long, R., Shen, L., Jagota, A., Hui, C.-Y., 2009. Effect of rate on adhesion and static friction of a film-terminated fibrillar interface. Langmuir 25, 2765–2771.
Varenberg, M., Gorb, S., 2007. Shearing of fibrillar adhesive microstructure: friction and shear-related changes in pull-off force. J. R. Soc. Interface 4, 721–725.
Waters, J.F., Lee, S., Guduru, P.R., 2009. Mechanics of axisymmetric wavy surface adhesion: JKR–DMT transition solution. Int. J. Solids Struct. 46, 1033–1042.
Yao, H., Gao, H., 2010. Gibson-soil-like materials achieve flaw-tolerant adhesion. J. Comput. Theor. Nanosci. 7, 1299–1305.
Yoon, H., Kwak, M.K., Kim, S.M., Sung, S.H., Lim, J., Suh, H.S., Suh, K.Y., Char, K., 2011. Polymeric nanopillars reinforced with metallic shells in the lower stem region. Small 7, 3005–3010.